Arene–Metal-Ion Contact: A Multicolor and Ratiometric Fluorescence Sensing Platform for Metal Ions

Anna Kanegae
Kyushu University
Yusuke Takata
Kyushu University
Ippei Takashima
Kyushu University
Shohei Uchinomiya
Kyushu University
Ryosuke Kawagoe
Kyushu University
Kazuteru Usui
Kyushu University
Jirarut Wongkongkatep
Mahidol University
Manabu Sugimoto
Kumamoto University
Akio Ojida (ojida@phar.kyushu-u.ac.jp)
Kyushu University https://orcid.org/0000-0002-9440-8167

Article

Keywords: metal ions, fluorescence sensing, ratiometric detection

Posted Date: August 14th, 2020

DOI: https://doi.org/10.21203/rs.3.rs-55176/v1

Version of Record: A version of this preprint was published at Communications Chemistry on July 6th, 2021. See the published version at https://doi.org/10.1038/s42004-021-00541-y.

Arene–Metal-Ion Contact: A Multicolor and Ratiometric Fluorescence Sensing Platform for Metal Ions

Anna Kanegae,[1,4] Yusuke Takata,[1,4] Ippei Takashima,[1] Shohei Uchinomiya,[1] Ryosuke Kawagoe,[1] Kazuteru Usui,[1] Jirarut Wongkongkatep,[2] Manabu Sugimoto,[3] Akio Ojida*[,1]

[1]Graduate School of Pharmaceutical Sciences, Kyushu University, Maidashi, Higashi-ku, Fukuoka, Japan

[2]Department of Biotechnology, Faculty of Science, Mahidol University, Rama 6 Road, Bangkok, Thailand

[3]Department of Science and Technology, Graduate School of Kumamoto University, Kurokami, Chuo-ku, Kumamoto, Japan

[4]These authors contributed equally: Anna Kanegae and Yusuke Takata

email: ojida@phar.kyushu-u.ac.jp

ABSTRACT: Despite continuous active development of fluorescent probes for metal-ions, their molecular design for ratiometric detection is limited owing to a narrow choice of available sensing mechanisms. We present herein a dual-emission sensing platform for metal ions based on contact interaction between a coordinated metal ion and the aromatic ring of a fluorophore (*i.e.*, arene–metal-ion contact). Our structure-based ligand design provided a new probe possessing 1,9-bis(2′-pyridyl)-2,5,8-triazanonane as the metal ion binding unit, which was flexibly concatenated to a tricyclic fluorophore. This molecular architecture allowed us to fluorescently sense various metal ions such as Zn(II), Cu(II), Cd(II), Ag(I), and Hg(II) with the red-shifted emissions. This probe design was applicable to a series of tricyclic fluorophores, enabling ratiometric detection of the metal ions across the blue to near-infrared wavelength region. X-ray crystallography and theoretical computational calculation indicated that the coordinated metal ion has van der Waals contact with the fluorophore, which perturbs its electronic structure and ring conformation to induce the emission red-shift. A set of the arene–metal-ion contact probes was used for the differential sensing of eight metal ions in a one-pot single titration via principal component analysis. Furthermore, the probe with a xanthene fluorophore was applicable to the ratio imaging of metal ions under live-cell conditions.

Fluorescent molecular probes are essential research tools in many fields as they can provide sensitive and selective detection of chemical species in real time. Among their sensing targets, metal ions have attracted special interest because of their significant biological effects. For harmful, non-essential heavy metal ions (mercury, cadmium, lead, etc.), fluorescent probes serve as tools to understand their biological behaviors in animals and plants[1], which occur as a result of unwanted uptake from the environment. Indeed, the detection of these harmful metal ions in organisms has been the subject of biological research for the last thirty years, and extensive studies are still being done to elucidate their multiple biological actions associated with their toxic effects.[2,3] Meanwhile, monitoring toxic metal ion contamination in the environment is also an important task for preserving global health.[4] For biologically relevant metal ions (calcium, zinc, copper, iron, etc.), detection of their localization and stimuli-dependent concentration change in live cell and tissue contexts facilitates understanding of their physiological and pathological roles.[5-7]

Fluorescent probes for metal ions are typically designed by connecting a coordination binding (ligand) unit to a luminescent sensing unit.[8] Design of the coordination ligand with high selectivity and tuned binding affinity for a target metal ion has been well developed as a result of the accumulated knowledge of coordination chemistry and supramolecular chemistry. Meanwhile, exploitation of new mechanism for metal ion sensing, which can effectively transduce the metal ion binding event to a fluorescence signal change, is still a challenging task.[9-10] The conventional and most widely used sensing mechanism for metal ions is PET (photoinduced electron transfer).[11] AIE (aggregation-induced emission)[12] and chemical reaction-based mechanisms (*i.e.*, activity-based sensing)[9,10,13] have also been exploited for metal ion sensing in recent years. In addition to these off-on type fluorescence sensing mechanisms, PCT (photoinduced charge transfer)[14] and FRET (fluorescence energy transfer)[15] have been used for the dual-emission ratiometric sensing of metal ions. However, they have rather limited utility as the former can only work with a limited class of fluorophores and the latter demands a complex probe structure owing to the necessity of using two fluorophores. Given these limitations that restrict broader application of fluorescent probes for quantitative and accurate ratiometric analysis,[16] there still exists a need for new molecular system for the ratiometric detection of metal ions. We envisioned that such new sensing system should (1) work flexibly with different types of fluorophores, (2) function effectively within simple molecular architectures, and (3) be broadly applicable to various metal ion sensing. These desirable functions would facilitate not only quantitatively detect various metal ions at a desired wavelength but also identification of a specific metal ion with high accuracy. In this article, we report the new ratiometric fluorescent probes for metal ions based on contact interaction between the coordinated metal ion and the aromatic ring of the fluorophore (*i.e.*, arene–metal-ion contact).

Introduction of a semicyclic ligand to a tricyclic fluorophore provided a designer probe, which forms an arene–metal-ion van der Waals contact (AM-contact) upon coordination to cause an emission red-shift. We found that this probe design is broadly applicable to various tricyclic fluorophores, the emissions of which cover a broad wavelength range of over 400 nm. A set of the AM-contact probes provided a multicolor fluorescence sensing system, which enabled us to distinguish several metal ions by one-pot single titration and principal component analysis (PCA). Probe with the xanthene fluorophore was also applicable to the ratiometric detection of various metal ions under live-cell conditions. These analytical applications demonstrate the broad utility of AM-contact sensing in fluorescence metal ion analyses.

Design of fluorescent probes

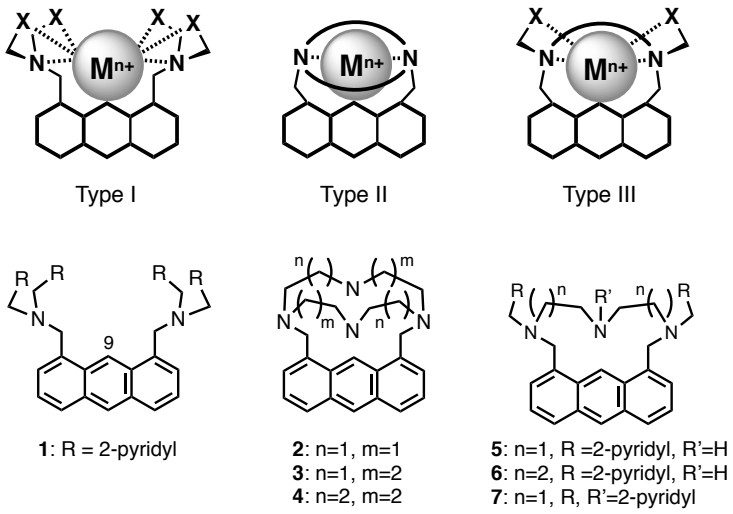

Figure 1. General designs (upper) and molecular structures (lower) of tricyclic fluorescent probes for metal ion sensing based on arene–metal-ion contact (AM-contact).

We previously reported that a Type-I probe serves as the ratiometric fluorescent chemosensor for metal ions based on AM-contact sensing (Figure 1).[17] For example, probe **1**, bearing two sets of 2,2′-dipicolylamine (*i.e.*, R = 2-pyridyl), exhibited a large emission red-shift upon binding with Cd(II), which was induced by forming van der Waals contact between the C9 carbon of the fluorophore and the metal ion in a 1:1 binding complex. However, while Type-I probes fluorescently responded to 4d- and 5d-block metal ions such as Cd(II), Ag(I), and Hg(II), they did not show an emission shift with 3d-block metal ions such as Zn(II). This limitation was mainly ascribed to the unfavorable formation of 1:2 binding complex with the rather small 3d-block metal ions at the ligand sites, which prohibited the van der Waals contact with the fluorophore. To solve this problem, we designed a Type-II probe (Figure 1) possessing a single tetra-aza cyclic ligand.[18,19] It was

expected that the Type-II probe would preferably form close van der Waals contact in a 1:1 metal ion complex. However, Type-II probes **2**–**4** were not able to fluorescently respond to most of the 3d-block metal ions such as Cr(II), Mn(II), Co(II), Ni(II), Zn(II), Ag(I), Cd(II), and Pb(II), with the exception of Cu(II) (Figure S1, Table S1). In the case of Cu(II), the probes decreased their fluorescence intensities without emission shift. We concluded that these unwanted results were primarily a result of the weak metal ion coordination ability of the conformationally constrained aza-cyclic ligands, which are concatenated to an anthracene ring at the 1,8-position. We next designed a Type-III probe, which possessed a conformationally more flexible semicyclic ligand (Figure 1). Probes **5**–**7**, each bearing a different semicyclic ligand, were synthesized according to standard methods, and their fluorescence response toward metal ions was evaluated under aqueous MeOH conditions (50 mM HEPES (pH 7.4)/MeOH = 1:1).

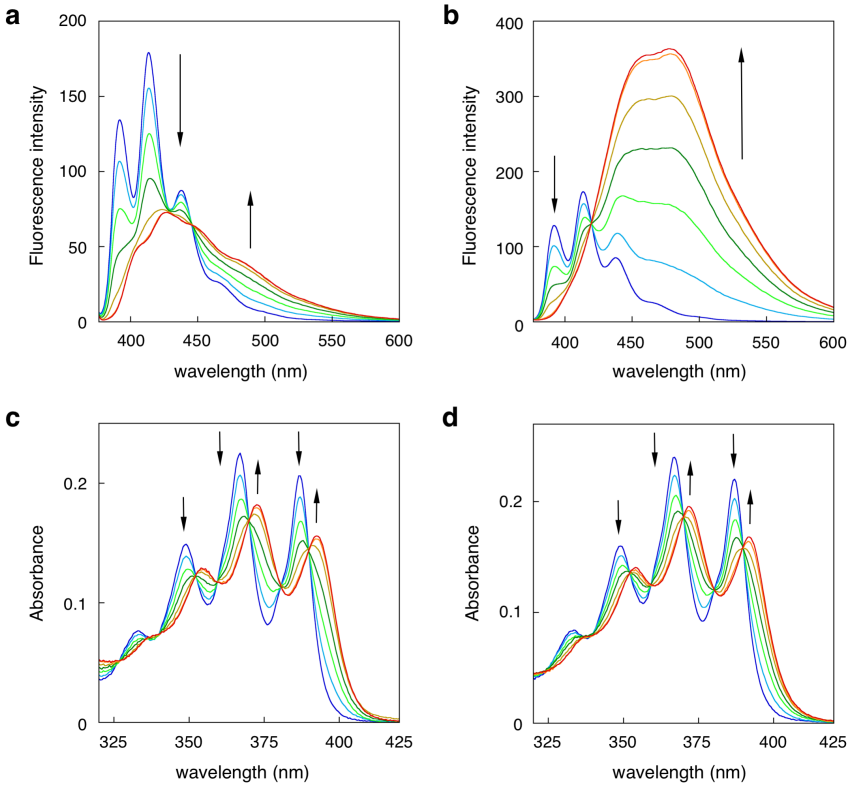

Figure 2. Fluorescence and absorption spectral changes of probe **5** upon addition of $ZnCl_2$ (**a** and **c**) or $CdCl_2$ (**b** and **d**). Measurement conditions: [**5**] = 25 μM, [$ZnCl_2$ or $CdCl_2$] = 0−30 μM, 50 mM HEPES (pH 7.4)/MeOH = 1:1, λ_{ex} = 365 nm, 25 °C.

To our delight, probe **5** bearing a 1,9-bis(2′-pyridyl)-2,5,8-triazanonane (BPTN) ligand exhibited a significant emission red-shift (ΔF = 14 nm) upon the addition of Zn(II) (Figure 2a). The fluorescence change of **5** was concomitant with a bathochromic absorption shift (ΔAbs = 6 nm) (Figure

2c), suggesting that the Zn(II) coordination influences the electrophysical property of the anthracene in the ground state. The fluorescence molar ratio plot clearly suggests that **5** forms a 1:1 binding complex with Zn(II) (Figure S2). The binding affinity of **5** to Zn(II) was 2.70×10^6 M^{-1} as evaluated by fluorescence titration (Figure S3, Table S2). Conversely, probes **6** and **7** showed negligible emission shift upon the addition of Zn(II) (Figure S4). Probe **5** also displayed a large emission red-shift (ΔF = 65 nm) and a bathochromic absorption shift (ΔAbs = 5 nm) (Figure 2b,d) upon complexation with Cd(II) ($K_a = 9.50 \times 10^6$ M^{-1}) (Figure S3, Table S2), while **6** and **7** showed smaller emission shifts (ΔF = 6 and 12.5 nm, respectively) compared with **5** (Figure S4).

Ratiometric sensing with various fluorophores

We next replaced the anthracene of **5** with other tricyclic fluorophores and evaluated the fluorescence sensing properties of this series of Type-III probes (Figure 3). Probes **8**–**11** possess the fluorophores coumarin, xanthene, pyronine, and Si-pyronine, respectively. The emission wavelengths of **5** and **8**–**11** cover a wide range from 380 to 800 nm. In addition to the difference in the emission wavelength, structural analysis of the fluorophores by density functional theory (DFT) suggested that the distance between the two methyl groups at their 1,8-positions (4,6-position in the case of coumarin **8**) varies from 4.64 to 5.21 Å (Figure 3). We expected that this structural difference could also affect the sensing and binding properties of the Type-III probes to metal ions. The detailed synthetic procedures and characterizations of the probes are described in the supporting information. The absorbance and fluorescence properties of the probes are summarized in Table 1.

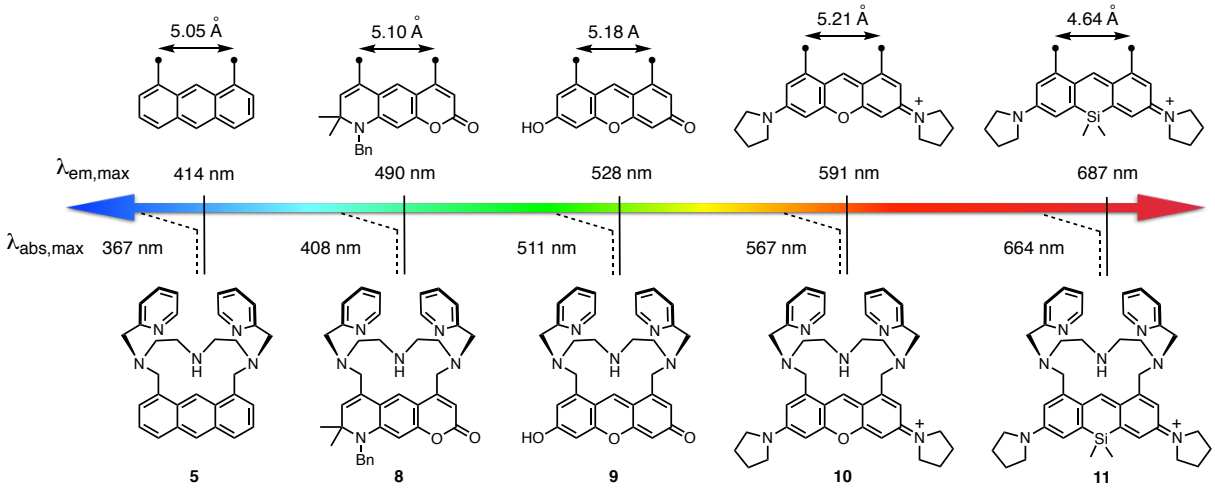

Figure 3. Structures and fluorescence spectroscopic properties of tricyclic fluorophore probes bearing a BPTN ligand.

Table 1. Summary of optical properties of Type-III probes **5** and **8**–**11**.[a]

	$\lambda_{abs,max}$ (nm)	ε ($cm^{-1} \cdot M^{-1}$)	$\lambda_{em,max}$ (nm)	Φ
5	367	8,500	414	0.03
8	408	19,500	490	0.50
9	511	66,000	528	0.24
10	567	138,000	591	0.53
11	664	138,500	687	0.30

[a]All measurements were conducted in 50 mM HEPES (pH 7.4)/MeOH = 1:1, 25 °C.

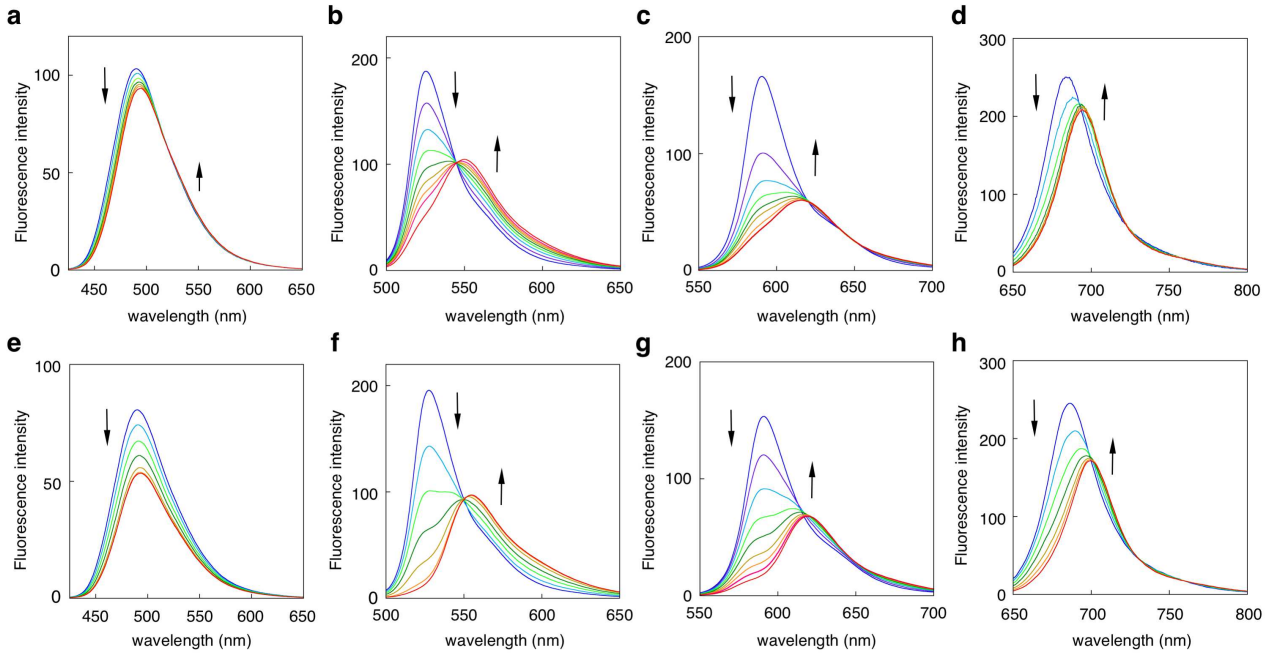

Figure 4. Fluorescence spectral changes of probes **8**–**11** (from left to right) upon addition of $ZnCl_2$ (**a**–**d**) or $CdCl_2$ (**e**–**h**). Measurement conditions: [probe] = 5 μM (**9**, **10**, **11**) or 10 μM (**8**), 50 mM HEPES (pH 7.4)/MeOH = 1:1, 25 °C.

Figure 4 shows the fluorescence spectra changes of **8**–**11** in titrations with Zn(II) and Cd(II) under aqueous MeOH conditions (50 mM HEPES (pH 7.4)/MeOH = 1:1). Xanthene **9** and pyronine **10** exhibited the largest emission red-shifts (ΔF = 27 and 25 nm, respectively) in the titration with Zn(II), while the wavelength shift of coumarin **8** was rather small (ΔF = 5 nm) (Table 2). Si-pyronine **11** exhibited a moderate emission red-shift (ΔF = 10 nm) in the near-infrared wavelength region (685 → 695 nm) upon coordination with Zn(II). The coordination of Cd(II) also induced a clear emission red-shift in the case of **9**, **10**, and **11** (ΔF = 27, 28, and 14 nm, respectively), while the wavelength shift of **8** was rather small (ΔF = 4 nm) as observed in the Zn(II) titration. It should be noted that all the probes showed bathochromic absorption shifts upon coordination with Zn(II)

and Cd(II) (Figure S5, Table S3). Interestingly, the binding affinity for Zn(II) varied depending on the fluorophore (Table S2). That is, anthracene **5** had the highest binding affinity (K_a = 2.7 × 10^6 M^{-1}), which is *ca.* 4- and *ca.* 50-fold stronger than that of xanthene **9** (K_a = 6.5 × 10^5 M^{-1}) and pyronine **10** (K_a = 5.0 × 10^4 M^{-1}), respectively. This binding affinity order was almost the same as that with Cd(II) (Table S2). The weak binding affinities of pyronine **10** could be ascribed to the long distance between the two 1,8-methylene carbons on the pyronine fluorophore (Figure 3), which may reduce the conformational flexibility of the BPTN ligand required for the coordination.

Table 2. Summary of fluorescence emission shifts of probes **5** and **8**–**11** upon addition of various metal ions.[a]

Probe	Cr^{3+}	Mn^{2+}	Co^{2+}	Ni^{2+} (1.63 Å)[b]	Cu^{2+} (1.40 Å)[b]	Zn^{2+} (1.39 Å)[b]	Ag^{+} (1.72 Å)[b]	Cd^{2+} (1.62 Å)[b]	Hg^{2+} (1.70 Å)[b]	Pb^{2+} (2.02 Å)[b]
5	-[c]	-[c]	<3	<3	<3	13	69	63	45	33
8	-[c]	-[c]	<3	<3	<3	5	<3	4	<3	<3
9	-[c]	-[c]	<3	<3 (3)[d]	25 (24)[d]	27 (25)[d]	8 (25)[d]	27 (25)[d]	34	<3
10	-[c]	-[c]	<3	<3	30	25	15	28	35	<3
11	-[c]	-[c]	8	<3	13	10	4	14	16	<3

[a]Fluorescence titration was conducted under aqueous MeOH conditions (50 mM HEPES (pH 7.4)/MeOH = 1:1). [b]Value in the parenthesis is the Van der Waals radius of metal ion. [c]Negligible fluorescence intensity change and emission shift were observed. [d]Value in the parenthesis is the fluorescence emission shift observed under aqueous buffer conditions (50 mM HEPES, pH 7.4).

We further investigated the fluorescence sensing properties of the probes toward other metal ions. All titrations were carried out under aqueous MeOH conditions (50 mM HEPES (pH 7.4)/MeOH = 1:1) to avoid aggregation of the metal complex. Table 2 and Figure S6 summarize the maximum emission red-shifts (ΔF) of **5** and **8**–**11** at the saturation point of the titration with metal ions. All the probes except for coumarin **8** showed significant emission red-shifts upon coordination with 4d- and 5d-block metal ions such as Ag(I), Cd(II), and Hg(II). In the titration with Cu(II), **9**–**11** also showed significant emission red-shifts along with a large decrease in the fluorescence (Figure S9–S11). Conversely, anthracene **5** did not show an emission shift upon binding with Cu(II) (Figure S7), even though a substantial bathochromic shift (ΔAbs = 6 nm) was observed in the absorption titration with Cu(II) (Table S3). This observation could be explained by a very weak fluorescence emission of the copper complex of **5** as a result of the strong quenching effect of Cu(II). Similarly, **5** and **11** showed negligible emission red-shifts in the titration with Ni(II) and Co(II), while their absorption wavelengths were clearly shifted (ΔAbs = 6–15 nm) (Table S3). The

metal ion titration was also conducted under aqueous buffer conditions (50 mM HEPES, pH 7.4) using the highly water-soluble probe **9**. Probe **9** exhibited a large emission red-shift upon binding with Cu(II), Zn(II), Ag(II), and Cd(II) (Table S2). The small emission red-shifts of coumarin **8** toward all the metal ions tested (Figure S8) might be attributed to the formation of an intramolecular charge transfer excited state, which cancels out the change in the photophysical property of the coumarin fluorophore induced by AM-contact. Another explanation for the small emission shifts of **8** might be an intrinsic low contact ability of the coumarin fluorophore because of its low electron density, as suggested by Hancock et al.[20]

X-ray structures of the metal ion complexes

The structures of the metal ion complexes of probe **5** were analyzed by X-ray crystallography (Figure 5, Figure S12, Table S4). The zinc complex **5**-Zn(II) has a square pyramidal coordination geometry and the five nitrogen atoms are coordinated to the Zn(II) ion (Figure 5a). The distance between Zn(II) and the adjacent C9 carbon atom is 2.96 Å, which is shorter than the sum of the van der Waals radii of Zn(II) (1.39 Å) and the aromatic carbon (1.77 Å) (Table S5).[21] Figure 5b is the cross-sectional view of the 5-Zn(II) complex, which clearly shows the van der Waals contact between the Zn(II) ion and the C9 carbon. Interestingly, this close contact induces bending of the C9−H bond by 6.9° from the π plane of the anthracene ring toward the side opposite of Zn(II). Van der Waals contact between the metal ion and fluorophore was also observed in **5**-Cd(II) and **5**-Ag(I) (Figure 5c,d). **5**-Cd(II) has a square pyramidal coordination geometry, and the distance between Cd(II) and the C9 carbon atom is 3.01 Å, which is shorter than the sum of the van der Waals radii of Cd(II) (1.58 Å) and the aromatic carbon (1.77 Å). **5**-Ag(I) has a trigonal pyramidal coordination geometry, in which one aliphatic nitrogen atom of the BPTN ligand does not coordinate to Ag(I). Although the distance between Ag(I) and the C9 carbon atom is rather long (3.28 Å), they still form a van der Waals contact owing to the large van der Waals radius of Ag(I) (1.72 Å). In contrast to **5**-Zn(II), the bending of the C9−H bond from the π plane of the anthracene ring in **5**-Cd(II) and **5**-Ag(I) is negligible. **5**-Cu(II) has a square planer coordination geometry, in which the distance between Cu(II) and the C9 carbon atom is 3.14 Å (Figure 5e). Although this distance is only slightly shorter than the sum of the van der Waals radii of Cu(II) (1.40 Å) and the aromatic carbon (1.77 Å), the coordination of Cu(II) induced the substantial absorption shift (ΔAbs = 6 nm) of **5** (Table S3). It is also worth noting that the conformation of the BPTN ligand is sufficiently flexible to coordinate metal ions with different radii; the distance between the N3′ nitrogen and N9′ nitrogen of the BPTN unit varied from 4.22 to 4.54 Å depending on the metal ion (Table S5),

accommodating the coordinated metal ions at the close position of the anthracene ring to induce the emission red-shift.

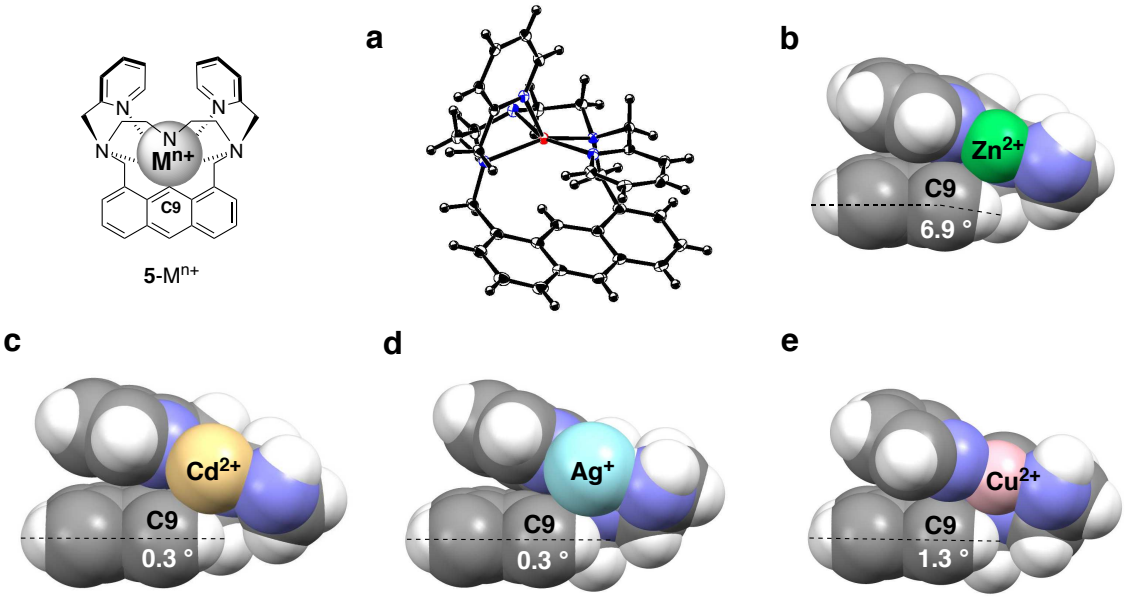

Figure 5. X-ray structures of the metal ion complexes **5**-M^{n+} (M^{n+} = Zn^{2+}, Cd^{2+}, Ag^{+}, or Cu^{2+}). (a) ORTEP diagram (50% probability ellipsoids) of **5**-Zn^{2+} ($C_{32}H_{32}N_4O_8Cl_2Zn$). The perchlorate anions are omitted for clarity. (b-e) Cross-sectional views of the metal ion complexes of **5**.

Computational analysis of AM-contact sensing

To understand the theoretical mechanism of AM-contact sensing, we performed electronic-structure calculations for the selected probes and their zinc ion complexes. The low-lying excited states of xanthene probe **9** and its zinc complex **9**-Zn(II) were initially calculated with the time-dependent density functional theory (TDDFT) method (Table 3). The $S_0 \rightarrow S_1$ transition energy of **9** was ΔE = 2.978 eV in water, which is smaller than that of **9**-Zn(II) (ΔE = 2.733 eV). This result reproduces the experimentally observed red-shift of the absorption band [2.426 eV (511 nm) → 2.380 eV (521 nm)] induced by Zn(II) ion coordination. Table S6 summarizes the HOMO and LUMO energy levels of **9** and **9**-Zn(II). The HOMO-LUMO energy gap of **9** (ΔE = 2.978 eV) decreases upon complexation with Zn(II) in water ($\Delta\Delta E$ = 0.245 eV). A TDDFT calculation was also conducted by replacing the zinc ion of **9**-Zn(II) with a positive charge (PC) of +1.0*e* (1PC) and +2.0*e* (2PC) (Table 3). The $S_0 \rightarrow S_1$ transitions of **9**+PC(1.0) and **9**+2PC(2.0) were calculated to be 2.827 and 2.360 eV, respectively, under vacuum conditions, which are lower than that of **9** (ΔE = 3.015 eV). The decrease of the $S_0 \rightarrow S_1$ transition energy was also induced by the coordination of other metal cations such as Na(I) and Ca(II) to **9** (Table S7). These results all suggest that electrostatic interaction with the positively charged Zn(II) influences the photophysical property

of **9**, leading to the coordination-induced emission red-shift in **9**-Zn(II). This prediction is consistent with that previously reported for the Cd(II) and Ag(I) complexes of the Type-I probes.[17]

Table 3. Summary of the S_0-S_1 excitation state of the probes with or without zinc ion/positive charge (PC) coordination.

species	optimized geometry[a]	environment	S_0-S_1 excitation		
			ΔE (eV)	λ (nm)	*f*
9	**9**	water[b]	2.978	416.3	0.808
9+Zn(II)	**9**	water[b]	2.733	453.6	0.618
9	**9**	vacuum	3.015	411.2	0.661
9+PC(0.0)	**9**-Zn(II)	vacuum	3.003	412.9	0.570
9+PC(1.0)	**9**-Zn(II)	vacuum	2.827	438.6	0.491
9+PC(2.0)	**9**-Zn(II)	vacuum	2.360	525.3	0.098
5	**5**	water[b]	3.596	344.8	0.163
5+Zn(II)	**5**	water[b]	3.520	352.2	0.152
5	**5**	vacuum	3.626	341.9	0.130
5+PC(0.0)	**5**-Zn(II)	vacuum	3.549	349.3	0.113
5+PC(1.0)	**5**-Zn(II)	vacuum	3.576	346.7	0.114
5+PC(2.0)	**5**-Zn(II)	vacuum	3.555	348.8	0.112

[a]Geometry optimization was performed for a molecule in vacuum. [b]The solvent effect was taken into account using the polarizable continuum model.

In the case of the anthracene probe **5**, the $S_0 \rightarrow S_1$ transition energy in water was calculated to be 3.596 eV (Table 3). This value was reduced to 3.520 eV in the zinc complex **5**-Zn(II). This trend in the narrowing of the energy gap agrees with the experimentally observed red-shift of the absorption band [3.378 eV (367 nm) → 3.324 eV (373 nm)] induced by zinc coordination. In the calculation with positive charge, the $S_0 \rightarrow S_1$ transition energy of **5**-PC(1.0) was calculated to be 3.576 eV under vacuum conditions, which is lower than that of **5** (ΔE = 3.626 eV) in vacuum. This result is consistent with the emission red-shift observed for the zinc coordination of **5**. Interestingly, when the calculation was conducted for **5**-PC(0.0), which possesses the optimized geometry of **5**-Zn(II) with a bent C9-H bond, the $S_0 \rightarrow S_1$ transition energy was calculated to be 3.549 eV. This value is smaller than that of **5**-PC(1.0) with the same geometry (ΔE = 3.576 eV), contradicting the experimental result of the zinc coordination of **5**. This implies that the emission red-shift of **5** can be induced not only by the electronic perturbation of the positively charged zinc ion, but also by the deformation of the anthracene ring as observed in the X-ray crystallography of **5**-Zn(II) (Figure 5b). This hypothesis was also proposed for the Ag(I) complex of a Type-II probe in our previous paper.[22]

Differential sensing of metal ions

Although the Type-III probes bearing a BPTN ligand can sense various metal ions, discrimination of individual metal ions is also of great importance in the fields of applied chemistry such as environmental monitoring, metal ion toxicology, and bioinorganic chemistry. In recent years, several types of fluorescence sensor arrays capable of distinguishing sets of metal ions have been reported.[23-26] These systems employ a series of cross-reactive sensors for metal ions, which produce a data set of the fluorescence signal change. Applying statistical analysis to the data enables unambiguous identification of the metal ions. We expected that the probes using AM-contact sensing would also be applicable to differential metal ion detection. In particular, we aimed to construct a one-pot multicolor fluorescence sensing system comprising a set of the probes, which fluoresce at different wavelengths. It was anticipated that this type of sensing system would allow us to avoid repeated measurements, which are usually necessitated in sensor array detection.

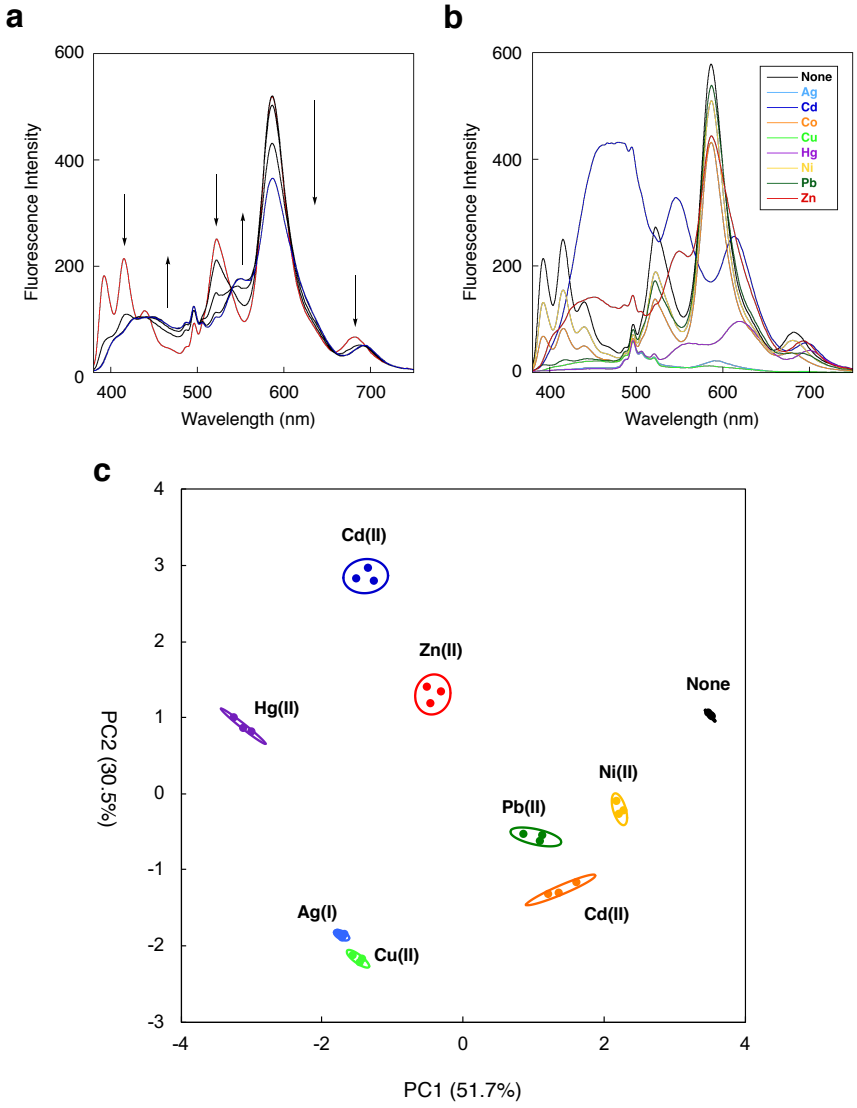

Figure 6. Multicolor fluorescence sensing of metal ions. (a) Fluorescence spectral change of the set of probes **5**, **9**, **10**, and **11** upon addition of $ZnCl_2$ (0−30 μM). (b) Fluorescence spectral change

of the set of probes upon addition of various metal ions (30 μM). (c) PCA plot of the two principle components (PC1 and PC2) for eight metal ions (30 μM). Measurement conditions: [**5**, **9**, **10**] = 2 μM, [**11**] = 4 μM, 50 mM HEPES (pH 7.4)/MeOH = 1:1, 25 °C. λ_{ex} = 254 nm.

As a proof-of-concept experiment, we employed the probes **5**, **9**, **10**, and **11** for multicolor metal ion sensing. A solution containing the set of probes (2 μM of **5**, **9**, and **10**, and 4 μM of **11**) displayed a complicated emission spectrum from 380 to 750 nm (Figure 6a) when excited at 254 nm. The addition of Zn(II) (0-30 μM) induced a clear spectral change as a result of the dual emission responses of each probe to provide a unique emission spectrum, which is distinct from the initial spectrum. Titration with other metal ions such as Co(II), Ni(II), Cu(II), Cd(II), Ag(I), Hg(II), and Pb(II) also provided the unique emission spectral changes (Figure 6b). Each spectral pattern was recorded at eight wavelengths to provide emission ratio values of F_{450}/F_{414}, F_{550}/F_{525}, F_{615}/F_{589}, and F_{690}/F_{679}, as well as emission intensity change F/F_o values at 414, 525, 589, and 679 nm as a set of signal outputs. By analyzing these data set using PCA, we were able to differentiate the eight metal ions at 30 μM on a two-dimensional dispersion graph (Figure 6c). PCA analysis was further applied to the output data of the concentration-dependent fluorescence spectral change. The two-dimensional dispersion graph revealed that the probe set can distinguish the four metal ions Zn(II), Cu(II), Cd(II), and Hg(II) in concentrations from 1 to 30 μM (Figure S13).

Ratio imaging of metal ions in live cells

We next set out to examine the utility of the xanthene-type probe for ratiometric fluorescence imaging of metal ions in living cells (Figure 7). For this purpose, we designed probe **12**, which possesses the lipophilic O-*p*-acetoxy benzyl and N-ethoxyethyl groups (Figure 7a). These substituents were introduced to increase the membrane permeability of **9**. We confirmed that probe **13**, which is obtained from **12** by hydrolysis, exhibits a clear dual emission change and a significant increase of the fluorescence intensity ratio (F_{550nm} / F_{520nm}) upon addition of $ZnCl_2$ under the neutral aqueous solution (50 mM HEPES, 100 mM NaCl, pH 7.4) (Figure 7b, 7c). The binding affinity of **13** toward Zn(II) was evaluated to be 6.1 x 10^6 M^{-1} under the same aqueous conditions (Figure S14). When HeLa cells were treated with 5 μM of **12** in HBS buffer, bright fluorescence from the xanthene fluorophore was observed inside the cells (Figure 7d). It was evident that non-fluorescent **12** penetrated into the cells and was hydrolyzed to fluorescent **13** by intracellular esterase. Treatment of the cells with 5 μM of zinc chloride in the presence of pyrithione (100 μM) induced a significant fluorescence increase at 540–630 nm ($F_{540\text{-}630\ nm}$). Ratiometric fluorescence analysis revealed that the ratio value ($F_{540\text{-}630\ nm}/F_{500\text{-}530\ nm}$) gradually increased in a time-dependent manner.

Live-cell imaging was further conducted for other metal ions such as Cu(II), Cd(II), and Hg(II). As shown in Figure 7e, the fluorescence ratio was changed inside the cells upon the addition of 5 μM of Cd(II) and Cu(II), while the change was rather small in the case of Hg(II). These results demonstrated that AM-contact sensing works in living cells to enable ratio imaging of the metal ions.

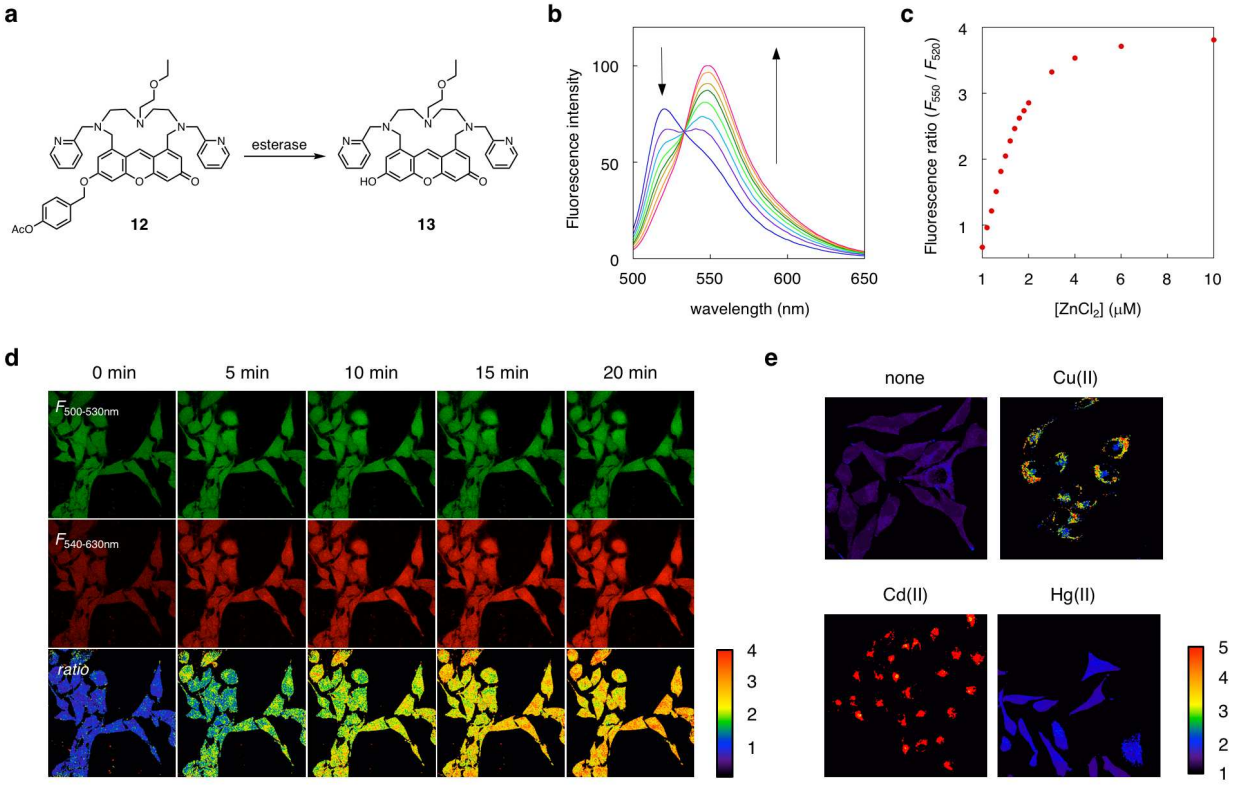

Figure 7. Ratiometric fluorescence detection of metal ions in living cells. (a) Structures of probe **12** and its hydrolyzed product **13**. (b) Fluorescence spectral change of **13** upon addition of $ZnCl_2$. Measurement conditions: [**13**] = 1 μM , [$ZnCl_2$] = 0, 0.2, 0.4, 0.6, 0.8, 1.0, 1.4, 2 μM, 50 mM HEPES 100 mM NaCl, pH 7.4, 25 °C, λ_{ex} = 488 nm. (c) Plot of the fluorescence intensity ratio (F_{550nm} / $F_{520\,nm}$) of **13** upon addition of $ZnCl_2$. (d) Time-lapse images of Zn(II) inside HeLa cells. The cells were incubated with probe **12** (5 μM) followed by the treatment with $ZnCl_2$ (5 μM) in the presence of pyrithione (100 μM). The ratio images were obtained from the imaging data acquired at two detection channels ($F_{540\text{-}630\,nm}$ and $F_{500\text{-}530\,nm}$). (e) Ratiometric detection of various metal ions in HeLa cells. The fluorescence images were acquired at 5 min after the treatment of the cells with each metal ion (5 μM) in the presence of pyrithione (100 μM).

Discussion

Chelation-induced PCT is the most widely used sensing mechanism in the development of ratiometric fluorescent probes for metal ions. In a probe implemented with this mechanism, the

fluorophore must have a heteroatom (N, O, S, etc.) directly connected to or incorporated in its π-electron system, which undergoes a change in its electronic structure upon coordination with a metal ion, resulting in an emission wavelength shift. Unfortunately, this structural requirement limits the choice of fluorophores available for the ratiometric fluorescence sensing of metal ions. FRET is less frequently employed in the design of ratiometric fluorescence probes for metal ions because the FRET system requires two fluorophores within one molecule, making it difficult to design a probe with the proper function. The large molecular size of the FRET-type probe also inhibits its aqueous solubility and cell membrane permeability in live-cell imaging. In contrast to these existing systems, AM-contact sensing does not have such structural limitations and requirements because it utilizes the spatial proximity between the fluorophore and metal ion, allowing a variety of fluorophores to be employed in a simple molecular architecture. Indeed, we clearly demonstrated in this study that AM-contact sensing could operate with various tricyclic fluorophores bearing a BPTN ligand.

Our previous results[17,22] and reports by Czarnik[27] and Hancock[20,28,29] suggested that the contact-induced emission shift was limited to rather large 4d- and 5d-block metal ions such as Cd(II) and Ag(I). In this paper, we demonstrated for the first time that AM-contact sensing could also work with the smaller 3d-block metal ions such as Zn(II) and Cu(II). This was possible due to the molecular design of the Type-III probe, which employs the semicyclic BPTN as a metal ligand unit. X-ray crystallography of the metal ion complexes of **5** revealed that the BPTN ligand places a metal ion on the upper edge of the anthracene π-plane to facilitate van der Waals contact between them. Computational analysis suggested that electrostatic interaction between the fluorophore and the adjacent metal ion largely contributes to the emission red-shift (Figure 5). It is reasonable to assume that this electrostatic interaction can effectively work in a coordination complex wherein the metal ion is located close to the fluorophore, within their van der Walls radii. The computational analyses further suggested that the bend of the C9-H bond in the anthracene ring, which was observed in the zinc complex of **5**, also contributes to the emission red-shift as a result of the change in the electronic structure of the fluorophore. We propose at this stage that these two structural perturbations (*i.e.*, electrostatic interaction with metal ion and deformation of aromatic ring) contribute to the emission shift in AM-contact sensing using the Type-III probes.

We have demonstrated the utility of AM-contact sensing in two analytical applications: multi-color differential sensing of metal ions based on PCA analysis and ratio imaging of metal ions in living cells. Both applications took full advantage of the unique properties of AM-contact sensing, including high compatibility with various fluorophores, broad applicability to different metal ions, and a clear ratiometric emission change. We expect that further refinement of the probe architecture, especially in the metal binding unit, will provide more sophisticated fluorescent probes with larger emission shifts and higher metal ion selectivities. We also envision that AM-contact sensing will be applicable to a broader range of metal ions, including alkaline and alkaline-earth metal ions, under

various analytical settings.[30] Finally, we envisage that the utility of AM-contact sensing can be further extended to the dual-emission sensing of anions[31] and organic molecules[32] if their coordination to the metal ion can perturb close contact between the fluorophore and the coordinated metal ion.

Methods

Metal ion titration

Fluorescence spectrum was recorded on PerkinElmer LS-55 spectrofluorophotometer. Absorption spectrum was measured using Shimadzu UV-2600 spectrophotometer. In typical titration experiment, probe solution (25 μM of **5**, 10 μM of **8**, or 5 μM of **9**, **10**, **11**) in 50 mM HEPES buffer (pH = 7.4) : MeOH = 1 : 1 was titrated with aqueous stock solution of metal ion in a quartz cell at 25 °C. The fluorescence and absorption spectra were measured at 5 min after addition of the metal ion at each titration point. In the fluorescence titration, probes **5**, **8**, **9**, **10**, **11** were excited at 365, 410, 488, 578, 674 nm, respectively. The plot of the fluorescence intensity at the maximum emission wavelength was analyzed by nonlinear least-square curve fitting to obtain the binding constant (K_a, M^{-1}).

Determination of fluorescence quantum yield (Φ)

Fluorescence quantum yields (Φ) of the probes were determined in 50 mM HEPES buffer (pH = 7.4) : methanol = 1 : 1 using quinine sulfate (Φ = 0.55) for **5** and **8**, fluorescein (Φ = 0.95) for **9**, Rhodamine 6G (Φ = 0.95) for **10** and NileBlue (Φ = 0.95) for **11** as the fluorescence quantum yield standards.

Multicolor fluorescence sensing of metal ions

Metal ion titration was carried out in aqueous-methanol solvent (50 mM HEPES buffer (pH = 7.4) : methanol = 1 : 1) containing the set of the probes (2 μM of **5**, **9**, **10** and 4 μM of **11**). After addition of the metal ions, the fluorescence spectra were recorded on PerkinElmer LS-55 spectrofluorophotometer at 25 °C (λ_{ex} = 254 nm). Principal component analysis (PCA) was performed with Microsoft Excel 2011 using the data set of the emission intensity change (F/F_0 at 414, 525, 589, 679 nm) and the emission ratios (F_{450}/F_{414}, F_{550}/F_{525}, F_{615}/F_{589}, F_{690}/F_{679}).

X-ray crystallography

All the metal ion complexes of **5** were crystallized from MeOH/CH_3CN = 3 : 1 at 30 °C. The X-ray data were collected on a Bruker AXS APEX II diffractometer with graphite monochromated MoKa radiation (λ = 0.71069 Å). The structures were solved by the direct method and refined anisotropically for non-hydrogen atoms by full-matrix least-squares calculations. The crystallographic calculations were performed by using the Crystal structure software package of the Rigaku Corporation. The CCDC deposition numbers of the crystallographic data are as follows: **5**-Zn(II); 1993118, **5**-Cd(II); 1993119, **5**-Ag(I); 1993120, **5**-Cu(II); 1993121.

Theoretical computational analysis

Density functional theory (DFT) was applied to investigate the electronic origin of the spectral shift induced in the metal complexes. In the calculation, the CAM-B3LYP functional was applied to describe the exchange-correlation term. This calculation was carried out for molecules in a vacuum with the default computational parameters in Gaussian09. In order to calculate the excited states, the TDDFT method was applied to obtain the lower 20 states. The Kohn–Sham orbitals were described with the Gaussian basis sets. For all the elements, we used the 6-31G(d,p) and the 6-31+G(d,p) basis sets for optimization. The solvent effect was taken into account by using the polarized continuum model for water as the solvent.

Cell culture

HeLa cells were cultured in high-glucose Dulbecco's Modified Eagle medium (DMEM, 4.5 g of glucose/L, Sigma-Aldrich) supplemented with 10% fetal bovine serum (FBS), penicillin (100 units/mL) and streptomycin (100 μg/mL) under humidified atmosphere of 5% CO_2 in air. Subculture was performed every 3-4 days from subconfluent (~ 80%) cultures using trypsin-EDTA solution.

Ratiometric fluorescence imaging of metal ions in living cells

HeLa cells ($1x10^5$) were cultured on 3.5 cm glass-based dish (Iwaki) for 2 days at 37 °C in CO_2 incubator. The cells were washed with HBS (20 mM HEPES, 107 mM NaCl, 6 mM KCl, 1.2 mM $MgSO_4$, 2 mM $CaCl_2$, 11.5 mM glucose, adjusted to pH 7.4 with NaOH) twice and pre-treated with probe **12** (5 μM) in HBS(+) for 20 min at 37 °C. After washed with HBS (+), the cells were treated with HBS containing pyrithione (100 μM) and each metal ion (5 μM) for 30 min at 37 °C and subjected to fluorescence imaging with confocal microscopy (TCS SP8, Leica Microsystems) equipped with HyD detector (λ_{ex} = 488 nm).

Data availability

The authors declare that all data supporting the findings of this study are available within the article and Supplementary Information files, and from the corresponding author on request.

References

1. Kim, H. N.; Ren, W. X.; Kim, J. S.; Yoon, J., Fluorescent and colorimetric sensors for detection of lead, cadmium, and mercury ions, *Chem. Soc. Rev.*, **41**, 3210-3244 (2012)
2. Rahman, Z.; Singh, V. P., The relative impact of toxic heavy metals (THMs) (arsenic (As), cadmium (Cd), chromium (Cr)(VI), mercury (Hg), and lead (Pb)) on the total environment: an overview, *Environ. Monit. Assess.*, 192:419 (2019).
3. Tchouwou, P. B., Yedjou, C. G.; Patlolla, A. K.; Sutton, D. J., Heavy metal ion toxicities and the

environment, Molecular, Clinical Environmental *Toxicology*, **101**, 133-164 (2012).
4. Dalmieda, J.; Kruse, P., Metal cation detection in drinking water, *Sensors*, **19**, 5134 (2019).
5. Que, E. L.; Bleher, R.; Duncan, F. E.; Kong, B. Y.; Gleber, S. C.; Vogt, S.; Chen, S.; Garwin, S. A.; Bayer, A. R.; Dravid, V. P.; Woodruff, T. K.; O'Halloran, T. V., Quantitative mapping of zinc fluxes in the mammalian egg reveals the origin of fertilization-induced zinc sparks, *Nat. Chem.*, **7**, 130-139 (2015).
6. Dodani, S. C.; Firl, A.; Chan, J.; Nam, C. I.; Aron, A. T.; Onak, C. S.; Ramos-Torres, K. M., Paek, J.; Webster, C. M.; Feller, M. B.; Chang, C. J., Copper is an endogenous modulator of neural circuit spontaneous activity, *Proc. Natl. Acad. Sci. USA*, **46**, 16280-16285 (2014).
7. Egawa, T.; Hanaoka, K.; Koide, Y.; Ujita, S.; Takahashi, N.; Ikegaya, Y.; Matsuki, N.; Terai, T.; Ueno, T.; Komatsu, T.; Nagano, T., Development of a far-red to near-infrared fluorescence probe for calcium ion and its application to multicolor neuronal imaging, *J. Am. Chem. Soc.,* **133**, 14157-14159 (2011).
8. Valeur, B.; Leray, I., Design principles of fluorescent molecular sensors for cation recognition, *Coord. Chem. Rev.*, **205**, 3-40 (2000).
9. Yeung, M. C.-L., Yam, V. W.-W., Luminescent cation sensors: from host-guest chemistry, supramolecular chemistry to reaction-based mechanism, *Chem. Soc. Rev.*, **44**, 4192-4202 (2015).
10. Aron, A. T.; Ramos-Tress, K. M.; Cotruvo, Jr., J. A.; Chang, C. J., Recognition- and reactivity-based fluorescent probes for studying transition metal signaling in living systems, *Acc. Chem. Res.*, **48**, 2434-2442 (2015).
11. Escudero, D., Revising intramolecular photoinduced electron transfer (PET) from first-principles, *Acc. Chem. Res.*, **49**, 1816-1824 (2016).
12. Li, Y.; Zhong, H.; Huang, Y.; Zhao, R., Recent advances in AIEgens for metal ion biosensing and bioimaging, *Molecules*, **24**, 4593 (2019).
13. Lake, R. J.; Yang, Z.; Zhang, J.; Lu, Y., DNAzymes as activity-based sensors for metal ions: recent applications, demonstrated advantages, current challenges, and future directions, *Acc. Chem., Res.*, **52**, 3275-3286 (2019).
14. Bourassa, D.; Elitt, C. M.; McCallum, A. M.; Sumalekshmy, S.; McRae, R. L.; Morgan, M. T.; Siegel, N.; Perry, J. W.; Rosenberg, P. A.; Fahrni, C. J., Chromis-1, A ratiometric fluorescent probe optimized for two-photon microscopy reveals dynamic changes in labile Zn(II) in differentiating oligodendrocytes, *ACS Sensors*, **3**, 458-467 (2018).
15. Park, S.-H.; Kwon, N.; Lee, J.-H.; Yoon, J.; Shin, I., Synthetic ratiometric fluorescent probes for detection of ions, *Chem. Soc. Rev.*, **49**, 143-179 (2020).
16. Grynkiewicz, G.; Poenie, M.; Tsien, R. Y., A new generation of Ca^{2+} indicators with greatly improved fluorescence properties, *J. Biol. Chem.*, **260**, 3440-3450 (1985).
17. Takashima, I.; Kinoshta, M.; Kawagoe, R.; Nakagawa, S.; Sugimoto, M.; Hamachi, I.; Ojida, A.,

Design of ratiometric fluorescent probes based on arene–metal-ion interactions and their application to CdII and hydrogen sulfide imaging in living cells, *Chem., Euro., J.*, **20**, 2184-2192 (2014).

18. Lee, H, N.; Kim, H. N., Swamy, K. M. K.; Park, M. S., Kim, J.; Lee, H.; Lee, K.-H.; Park, S.; Yoon, J., New acridine derivatives bearing immobilized azacrown or azathiacrown ligand as fluorescent chemosensors for Hg^{2+} and Cd^{2+}, *Tetrahedron Lett.*, **49**, 1261-1265 (2008).
19. Fages, F.; Desvergne, J.-P.; Bouas-Laurent, H.; Marsau, P.; Lehn, J.-M.; Kotzyba-Hibert, F.; Albrecht-Gary, A.-M.; Al-Joubbeh, M., Anthraceno-cryptands: A new class of cation-complexing macrocycle fluorophores, *J. Am. Chem. Soc.*, **111**, 8672-8680 (1989).
20. Nugent, J. W.; Reibenspies, J. H.; Hancock, R. D., Controlling the fluorescence response of PET sensors via the metal-ion π-contacting ability of the fluorophore: coumarin, a weaker π-contacter, *Inorg. Chem.*, **54**, 9976-9988 (2015).
21. Bondi, A., van der Waals Volumes and Raddi, *J. Phys. Chem.*, 1964, 68, 441-451.
22. Takashima, I.; Kanegae, A.; Sugimoto, M.; Ojida, A., Aza-crown-ether-appended xanthene: selective ratiometric fluorescent probe for silver (I) ion based on arene–metal ion interaction, *Inorg. Chem.*, **53**, 7080-7082 (2014).
23. Smith, D. G.; Topolmicki, I. L.; Zwicker, V. E.; Jolliffe, K. A.; New, E. J., Fluorescent sensing arrays for cations and anions, *Analyst*, **142**, 3549-3563 (2017).
24. Sarkar, T.; Selvakumar, K.; Motiei, L.; Margulies, Message in a molecule, *Nat. Commun.*, 7:11374 (2016).
25. Yuen, L. H.; Franzini, R. M.; Tan, S. S.; Kool, E. T., Large-scale detection of metals with a small set of fluorescent DNA-like chemosensors, *J. Am. Chem. Soc.*, **136**, 14576-14582 (2014).
26. Palacios, M. A.; Wang, Z.; Montes, V. A.; Zyryanov, G. V.; Anzenbacher Jr., P., Rational Design of a minimal size sensor array for metal ion detection, *J. Am. Chem. Soc.*, **130**, 10307-10314 (2008).
27. Huston, M. E.; Engleman, C.; Czarnik, A. W., Chelatoselective fluorescence perturbation in anthrylazamacrocycle conjugate probes. Electrophilic aromatic cadmiation, *J. Am. Chem., Soc.*, **112**, 7054-7056 (1990).
28. Colenda, B. E.; Lee, H.-S.; Reibenspies, J. H.; Hancock, R. D., Indole-based fluorescence sensors for both cations and anions, *Inorg. Chim. Acta.*, **482**, 478-490 (2018).
29. Nugent, J. W.; Lee, H.; Lee, H.-S.; Reibenspies, J. H.; Hancock, R. D., The effect of □ contacts between metal ions and fluorophores on the fluorescent PET sensors: Implications for sensor design for cations and anions, *Inorg. Chem.*, **53**, 9014-9026 (2014).
30. Lenthall, J. T.; Steed, J. W., Organometallic cavitands: Cation-p interactions and anion binding via π-metallation, *Coord. Chem. Rev.*, **251**, 1747-1760 (2007).
31. Nugent, J. W.; Lee, H.; Lee, H.-S.; Reibenspies, J. H.; Hancock, R. D., Mechanism of chelation enhanced fluorescence in complexes of cadmium (II), and a possible new type of anion sensor, *Chem. Commun.*, 49, 9749-9751 (2013).

32. Hitomi, Y.; Nagai, T.; Kodera M., A silver complex with an N, S, S-macrocyclic ligand bearing an anthracene pendant arm for optical ethylene monitoring, *Chem. Commun.*, 48, 10392-10394 (2012).

Acknowledgements

This work was supported by the Grant-in-Aid for Scientific Research on Innovative Areas "Chemistry for Multimolecular Crowding Biosystems" (JSPS KAKENHI Grant No. JP17H06349) and the Grant-in-Aid for Scientific Research B (JSPS KAKENHI grant no. JP20H02861 to A. O.). A.O. acknowledges Naito Science Foundation and Toray Science Foundation for their financial supports. S.U. acknowledges Grant-in-Aid for Young Scientists B (JSPS KAKENHI Grant No. JP17K14518) for its financial support.

Author contributions

A.O. designed the experiments. A.K., Y.T., I.T., S.U., and R.K. performed the experiments. U.K. and M.S. performed the computational theoretical analyses. A.O., J.W., and M.S. analyzed and discussed the data. The manuscript was written by A.O., J.W., and M.S.

Competing interests

The authors declare no competing interests.

Additional information

Supplementary information is available for this paper at

Figures

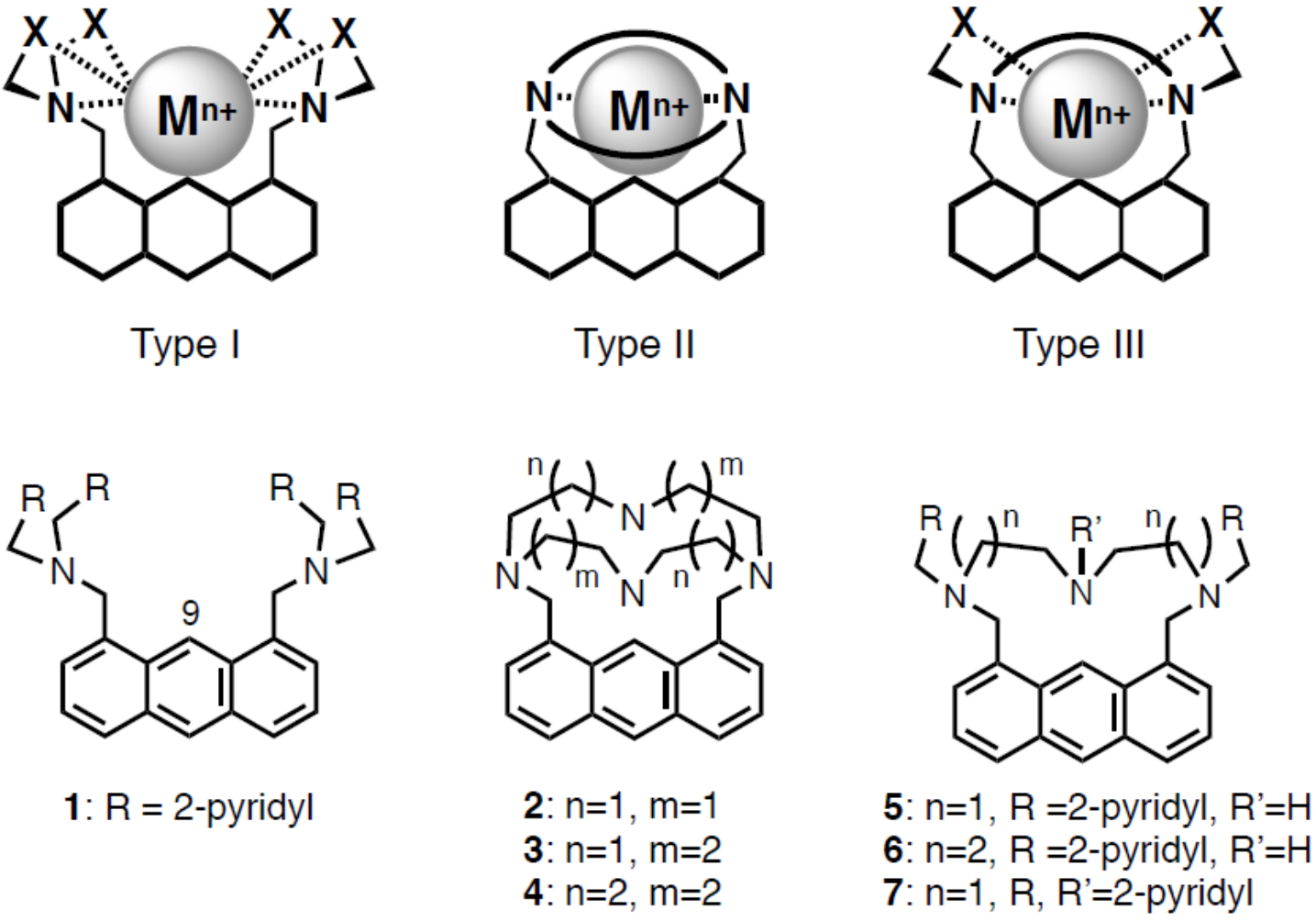

Figure 1

General designs (upper) and molecular structures (lower) of tricyclic fluorescent probes for metal ion sensing based on arene–metal-ion contact (AM-contact).

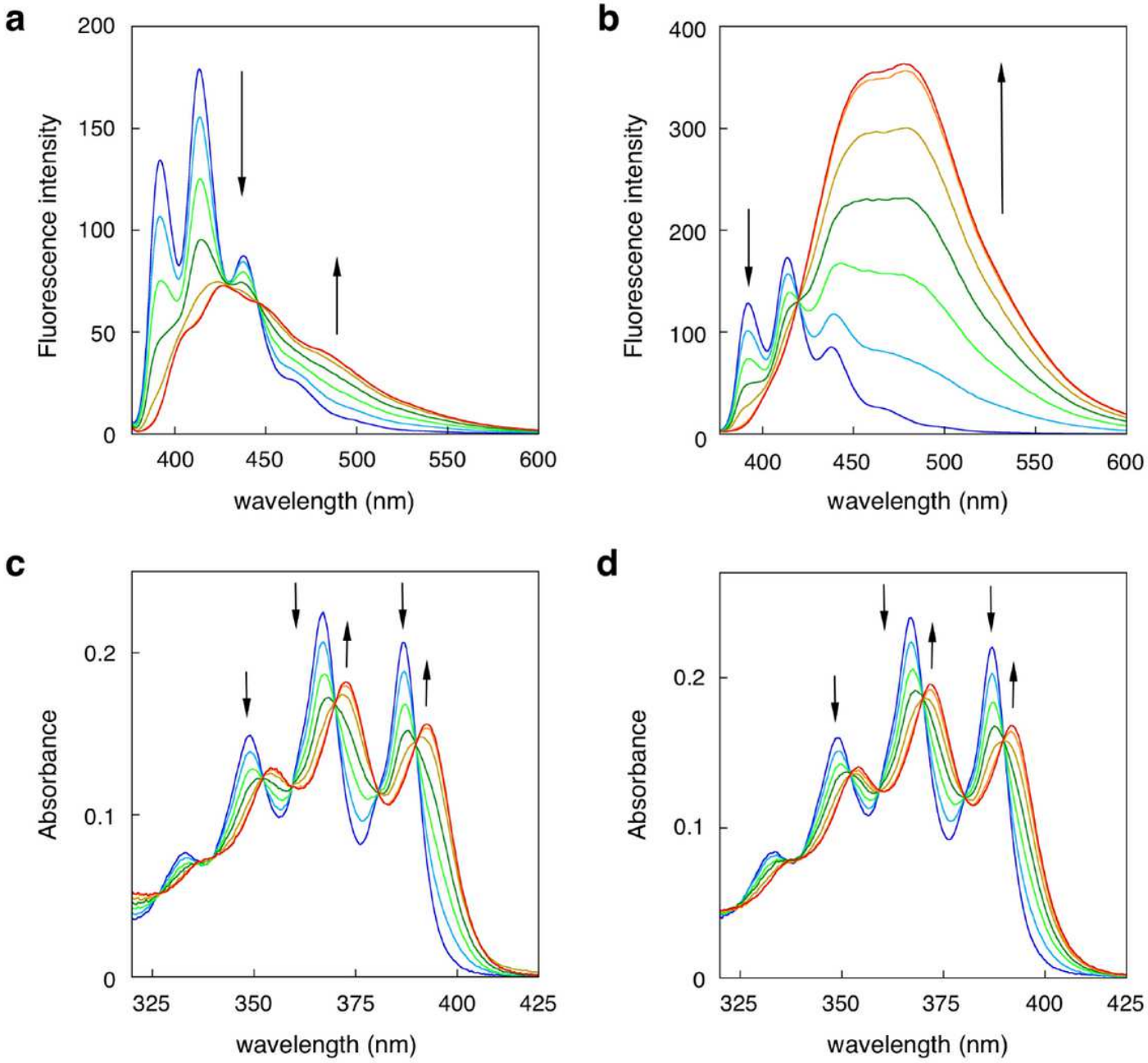

Figure 2

Fluorescence and absorption spectral changes of probe 5 upon addition of ZnCl2 (a and c) or CdCl2 (b and d). Measurement conditions: [5] = 25 μM, [ZnCl2 or CdCl2] = 0–30 μM, 50 mM HEPES (pH 7.4)/MeOH = 1:1, lex = 365 nm, 25 °C.

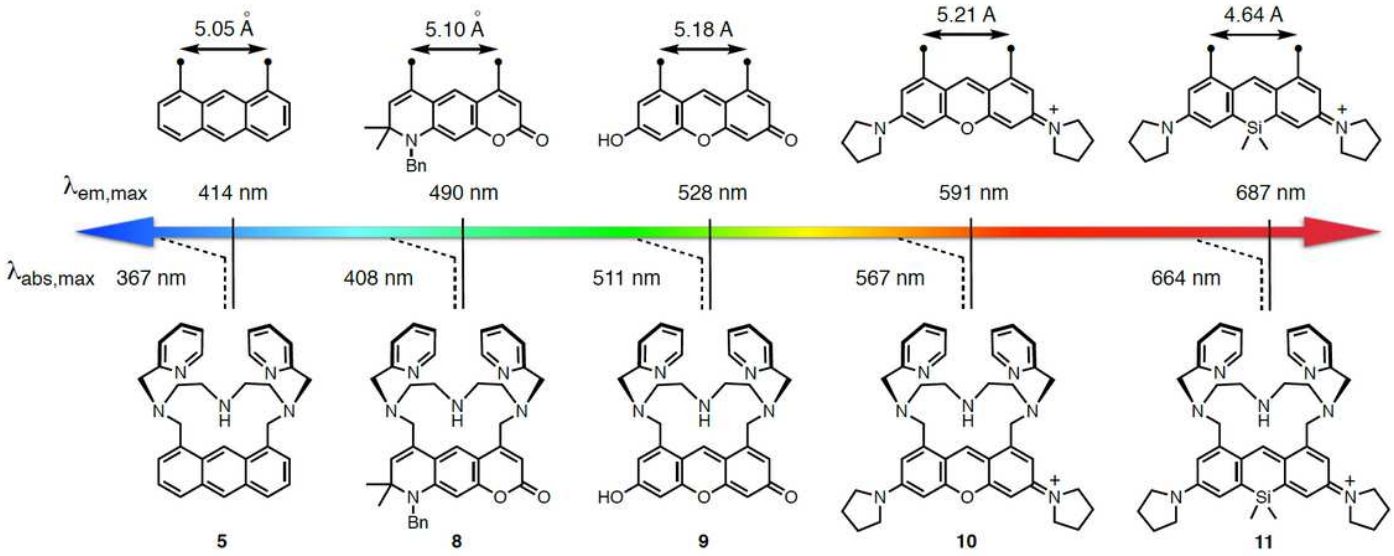

Figure 3

Structures and fluorescence spectroscopic properties of tricyclic fluorophore probes bearing a BPTN ligand.

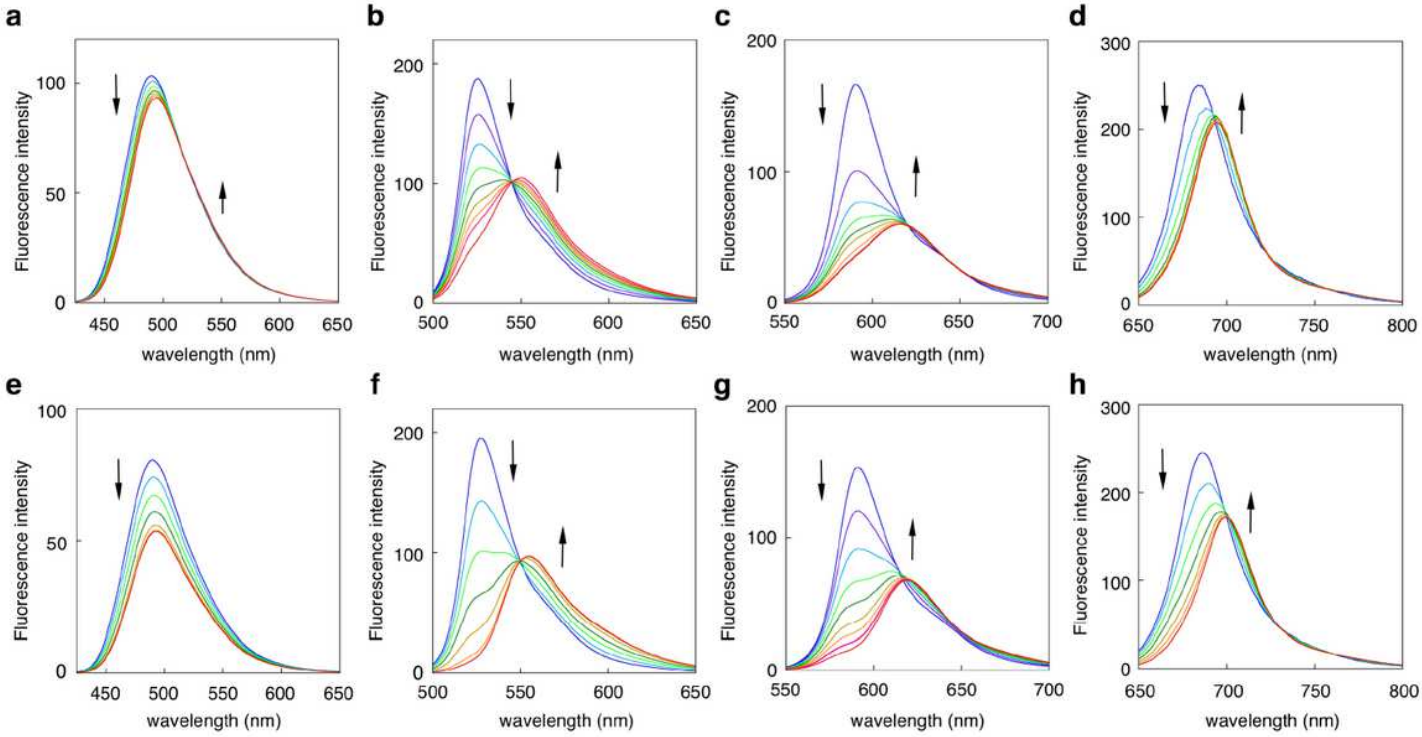

Figure 4

Fluorescence spectral changes of probes 8–11 (from left to right) upon addition of ZnCl2 (a–d) or CdCl2 (e–h). Measurement conditions: [probe] = 5 μM (9, 10, 11) or 10 μM (8), 50 mM HEPES (pH 7.4)/MeOH = 1:1, 25 °C.

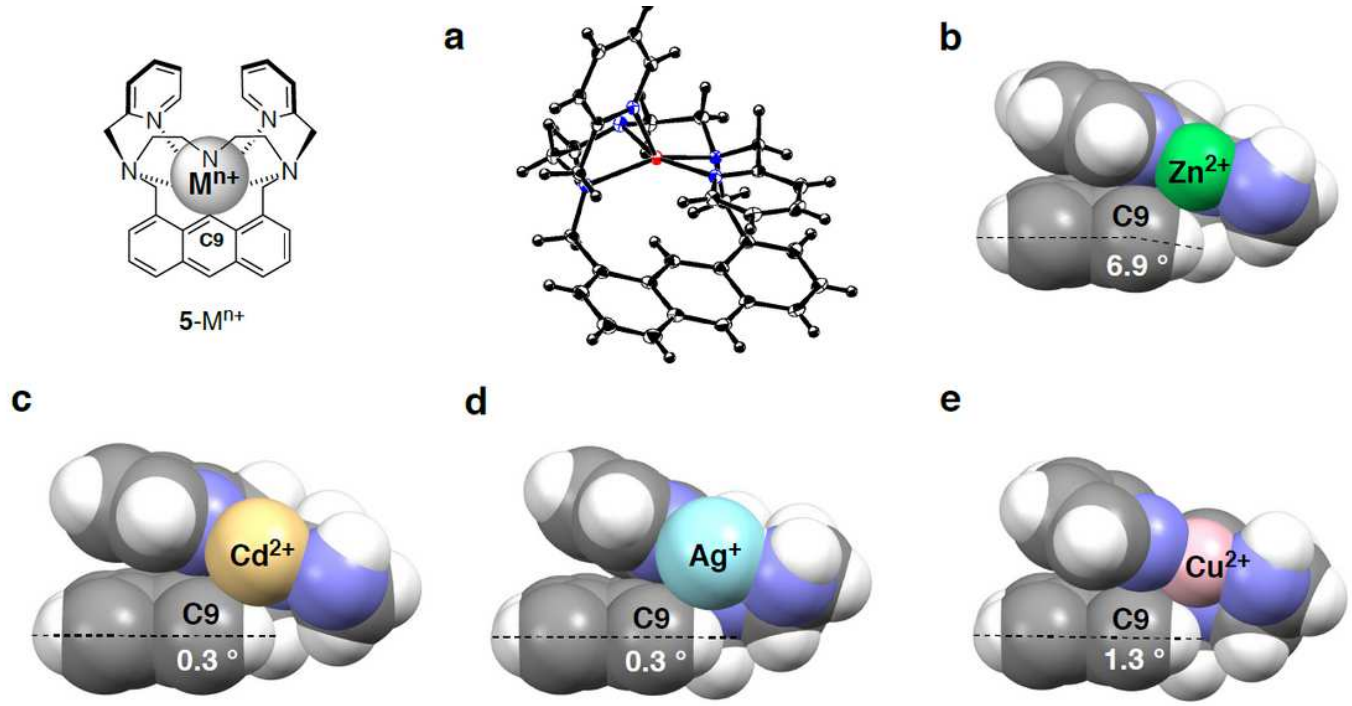

Figure 5

X-ray structures of the metal ion complexes 5-Mn+ (Mn+ = Zn2+, Cd2+, Ag+, or Cu2+). (a) ORTEP diagram (50% probability ellipsoids) of 5-Zn2+ (C32H32N4O8Cl2Zn). The perchlorate anions are omitted for clarity. (b-e) Cross-sectional views of the metal ion complexes of 5.

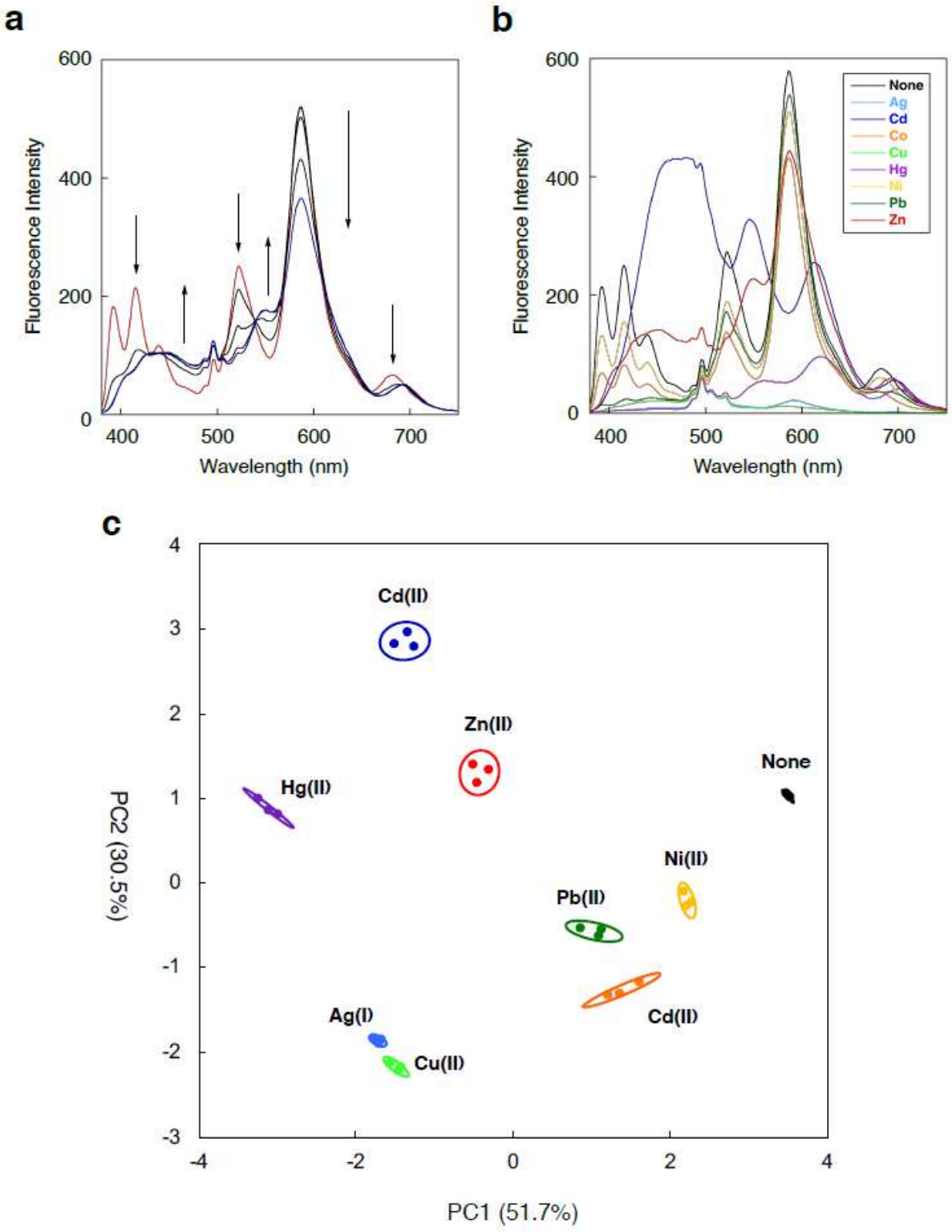

Figure 6

Multicolor fluorescence sensing of metal ions. (a) Fluorescence spectral change of the set of probes 5, 9, 10, and 11 upon addition of ZnCl2 (0–30 μM). (b) Fluorescence spectral change of the set of probes upon addition of various metal ions (30 μM). (c) PCA plot of the two principle components (PC1 and PC2) for eight metal ions (30 μM). Measurement conditions: [5, 9, 10] = 2 μM, [11] = 4 μM, 50 mM HEPES (pH 7.4)/MeOH = 1:1, 25 °C. lex = 254 nm.

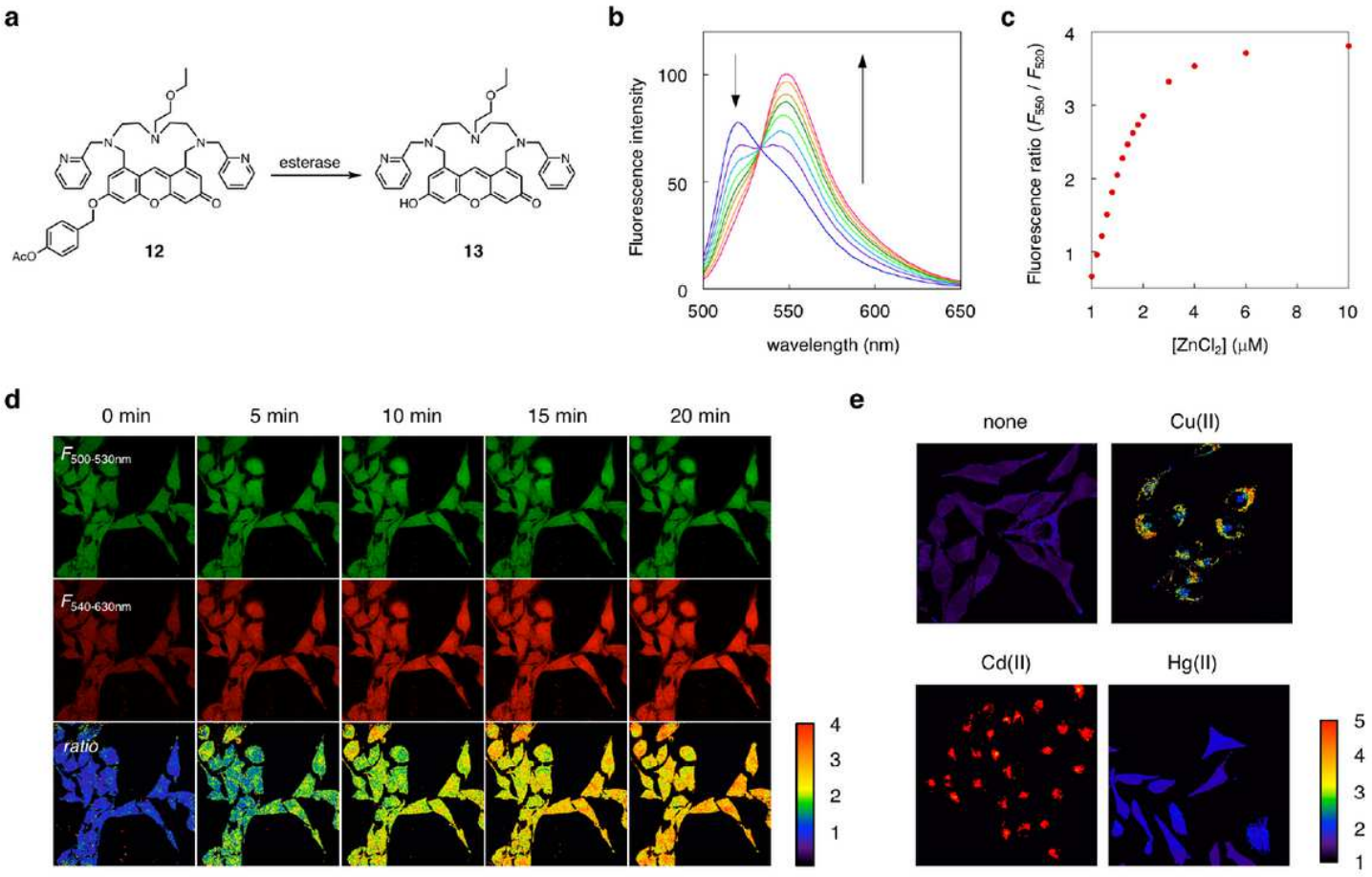

Figure 7

Ratiometric fluorescence detection of metal ions in living cells. (a) Structures of probe 12 and its hydrolyzed product 13. (b) Fluorescence spectral change of 13 upon addition of ZnCl2. Measurement conditions: [13] = 1 μM , [ZnCl2] = 0, 0.2, 0.4, 0.6, 0.8, 1.0, 1.4, 2 μM, 50 mM HEPES 100 mM NaCl, pH 7.4, 25 °C, lex = 488 nm. (c) Plot of the fluorescence intensity ratio (F550nm / F520 nm) of 13 upon addition of ZnCl2. (d) Time-lapse images of Zn(II) inside HeLa cells. The cells were incubated with probe 12 (5 μM) followed by the treatment with ZnCl2 (5 μM) in the presence of pyrithione (100 μM). The ratio images were obtained from the imaging data acquired at two detection channels (F540-630 nm and F500-530 nm). (e) Ratiometric detection of various metal ions in HeLa cells. The fluorescence images were acquired at 5 min after the treatment of the cells with each metal ion (5 μM) in the presence of pyrithione (100 μM).

Supplementary Files

This is a list of supplementary files associated with this preprint. Click to download.

- SupplementaryInfoCommunChem.pdf